

Article

Carbonation Resistance of Surface Protective Materials Modified with Hybrid NanoSiO₂

Kailun Xia ¹, Yue Gu ^{1,*}, Linhua Jiang ¹, Mingzhi Guo ¹, Lei Chen ¹ and Feilong Hu ²

¹ College of Mechanics and Materials, Hohai University, Nanjing 210098, China; xklhhu@hhu.edu.cn (K.X.); lhjiang@hhu.edu.cn (L.J.); mzguo@hhu.edu.cn (M.G.); chenyuanshi@hhu.edu.cn (L.C.)

² Suzhou Hechuan Chemical Technology Service Co., Ltd., Suzhou 215216, China; feihoo15@163.com

* Correspondence: gubetter@hhu.edu.cn

Abstract: To date, reinforcement concrete is the main construction material worldwide. As the concentration of atmospheric CO₂ is steadily increasing, carbonation of the reinforcement concrete becomes a pressing concern. In this study, novel surface protective materials (SPMs) modified with hybrid nanoSiO₂ (HNS), fly ash, and slag were developed to reduce CO₂ emissions and extend the service life of the reinforcement concrete. The carbonation depths were measured by phenolphthalein to reflect the carbonation resistance. X-ray diffraction (XRD), fourier-transform infrared spectroscopy (FTIR), and thermal gravimetric analysis (TGA) were conducted to analyze the chemical components of the samples after carbonation. In addition, MIP was carried out to examine the microstructures of the samples prior to carbonation. Thermodynamic modeling was employed to calculate the changes in the phase assemblages of each blends in an ideal situation. The experimental results showed that the carbonation depth and CaCO₃ content of the SPM modified with HNS decreased by 79.0% and 64.6% compared with the reference, respectively. The TGA results showed that after carbonation, the CaCO₃ contents were 4.40% and 12.42% in the HNS modified samples and reference samples, respectively. MIP analysis demonstrated that the incorporation of HNS in SPM led to a 48.3% and 58.5% decrease in big pores and capillary pores, respectively. Overall, the SPMs modified with HNS in this study possessed better carbonation resistance and refined pore structures.

Keywords: reinforcement concrete; carbonation; hybrid nanoparticles; pore structure



Citation: Xia, K.; Gu, Y.; Jiang, L.; Guo, M.; Chen, L.; Hu, F. Carbonation Resistance of Surface Protective Materials Modified with Hybrid NanoSiO₂. *Coatings* **2021**, *11*, 269. <https://doi.org/10.3390/coatings11030269>

Academic Editor: Junjie Wang

Received: 21 January 2021

Accepted: 20 February 2021

Published: 25 February 2021

Publisher's Note: MDPI stays neutral with regard to jurisdictional claims in published maps and institutional affiliations.



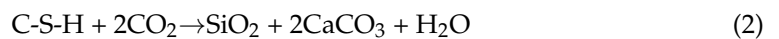
Copyright: © 2021 by the authors. Licensee MDPI, Basel, Switzerland. This article is an open access article distributed under the terms and conditions of the Creative Commons Attribution (CC BY) license (<https://creativecommons.org/licenses/by/4.0/>).

1. Introduction

Over the past decade, the concentration of CO₂ in the atmosphere has increased significantly [1], resulting in associated environmental pollution problems. As the binder of reinforcement concrete, cement has been widely used across the world. However, the production of cement generates a huge amount of anthropogenic CO₂ [2–4]. The cement industry as a whole accounts for about 5–8% of global CO₂ emissions. Thus, extending the service life of concrete is a viable strategy to reduce the demand of cement, which in turn will effectively cut the carbon footprint.

It is well-known that mature concrete has a tendency to react with the atmospheric CO₂ in natural environments. The carbonation of concrete is more prone to occurring upon exposure to a high concentrated CO₂ level, because CO₂ can readily diffuse into the pore solutions through a normally porous surface structure of concrete. The precipitation of CaCO₃ depletes Ca²⁺ in the pore solution, resulting in the release of Ca²⁺ from hydration products to maintain the dissolution equilibrium of calcium in the pore solution. This inevitably leads to changes in the hydration products. Among the hydration products, calcium hydroxide (CH) and calcium silicate hydrate (C–S–H) are the main reactants in the carbonation process (Equations (1) and (2)). For C–S–H, the depletion of Ca²⁺ tends to cause decalcification and decrease the Ca/Si ratio, forming decalcified C–S–H and eventually amorphous silica gel.





Another problem caused by the carbonation of concrete is the drop in the pH of the pore solution due to the neutralization reaction between carbonic acid and alkali. Under such a circumstance, the passive film on the steel surface has a propensity to undergo chloride-induced corrosion [5,6]. This poses a great threat to the durability of reinforcement concrete. Therefore, enhancing the carbonation resistance of reinforcement concrete represents an effective way to improve its durability and extend the service life.

In recent years, surface protective materials (SPMs) have attracted increasing attention as a feasible and economic way to prevent the diffusion of CO₂ into the inner parts of concrete, especially the vicinity of the reinforced steel [7,8]. On the other hand, supplementary cementitious materials (SCMs), such as fly ash and slag, are reported to be effective in augmenting the resistance of concrete to carbonation and chloride ingress [9]. At the same time, new cementitious binder materials composed of a high content of SCMs were referred to as lower carbon emission in cement manufacture [10]. Some researchers even found that some sorts of blast furnace slag can provide a better performance than the reference concrete [11]. This reasonably raises the question of whether the combination of SCMs with SPMs can synergistically enhance the carbonation resistance of reinforcement concrete. However, one downside of the addition of SCMs in cementitious material is the negative effect on the early strength [12]. NanoSiO₂ (NS) has been extensively investigated to evaluate its ability to compensate for the SCMs-induced adverse influence on the early-age properties [13,14]. As an inorganic agent for modifying cement-based materials, NS holds great potential for commercial applications due to its low cost and excellent properties. For example, NS can elicit a filling effect because it can act as a micro aggregate to fill the aperture between the cement particles and thereby densify the microstructures [15,16]. Moreover, NS also has a seeding effect by adsorbing calcium ions and serving as nucleation sites of C–S–H due to the large specific surface area [17]. Furthermore, NS can function as a pozzolana because it can react with CH to form C–S–H [18,19].

The above three effects of NS work together to improve the early mechanical properties of reinforcement concrete, such as flexural strength and compressive strength [20,21]. As nano particles, however, NS is prone to agglomeration in the pore solution in the presence of various positive ions. In contrast, hybrid nanoSiO₂ (HNS) is a novel nanoparticle which has better dispersion than traditional NS. For example, Gu et al. [22] synthesized a core-shell nanoparticle and found that the obtained hybrid NS was well dispersed in water and remained stable. Collodetti et al. [23] found that the siloxane modified nanoSiO₂ densified the nanostructure of Portland cement pastes, and coating siloxane on the surface enhanced the nanoSiO₂ stability in pore solutions. Mora et al. [24] developed novel hybrid silica particles functionalized with n-dodecyl groups (–C₁₂H₂₅) and found that they both had better dispersion and hydrophobicity. Therefore, hybrid nanoSiO₂ with an organic-inorganic core shell structure seems to be an effective additive to promote microstructure and durability of cement-based materials. Since surface is the first barrier to resist carbonation, coating the surface with SPMs is a cost-effective way to enhance the carbonation resistance of concrete.

In this paper, surface protective materials (SPMs) were prepared with the incorporation of two types of SCMs, i.e., fly ash and slag. In order to compensate for the adverse effect of SCMs on the early-age properties, a kind of hybrid nanoSiO₂ (HNS) with a core-shell structure was also added to the SPM. The carbonation depth of the SPM was measured to assess its carbonation resistance ability. X-ray diffraction (XRD), thermal gravimetric analysis (TGA), and fourier-transform infrared spectroscopy (FTIR) were employed to characterize the changes in the chemical compositions of the SPM before and after carbonation. Moreover, mercury intrusion porosimeter (MIP) was conducted to investigate the changes in the pore structures before carbonation in different blends. Finally, thermodynamic modeling was used to simulate the changes in phase assemblage, pH value, and Ca/Si ratios upon interacting with CO₂.

2. Materials and Methods

2.1. Materials

The cement used in all the experiments was Ordinary Portland Cement (OPC) compliant with the Chinese Nation Standard GB8076-2008 which was purchased from Anhui Conch Cement Co., Ltd. (Wuhu, China). Table 1 lists the chemical compositions of OPC characterized by XRF. The class F fly ash and blast furnace slag were used. The chemical compositions of the used fly ash and slag are listed in Tables 2 and 3, respectively. The aggregate used was purchased from China ISO Standard Sand manufactured according to ISO679: 1989, EN196-1.

Table 1. Chemical compositions of Ordinary Portland Cement (OPC).

Component	CaO	SiO ₂	Al ₂ O ₃	Fe ₂ O ₃	SO ₃	MgO	K ₂ O	L.O.I.
Content(wt%)	62.83	20.50	5.61	3.84	3.07	1.70	1.31	1.14

Table 2. Chemical compositions of fly ash.

Component	CaO	SiO ₂	Al ₂ O ₃	Fe ₂ O ₃	SO ₃	MgO	K ₂ O	L.O.I.
Content(wt%)	3.39	57.23	28.34	4.07	1.08	1.22	2.51	1.02

Table 3. Chemical compositions of slag.

Component	CaO	SiO ₂	Al ₂ O ₃	Fe ₂ O ₃	SO ₃	MgO	K ₂ O	L.O.I.
Content(wt%)	26.51	46.29	7.84	5.05	0.62	10.46	1.76	1.47

The commercially available hybrid nanoSiO₂ (HNS) was provided by Jiangsu Sobute New Materials Co., Ltd. (Nanjing, China). The inorganic constituent of HNS is nanoSiO₂ (NS), while the organic components in HNS are mainly the aliphatic molecular group, which accounts for 13% (by weight), according to the instructions provided by the supplier. The diameter of HNS ranged from 30 to 60 nm. The schematic diagram of the molecular structure of HNS is presented in Figure 1.

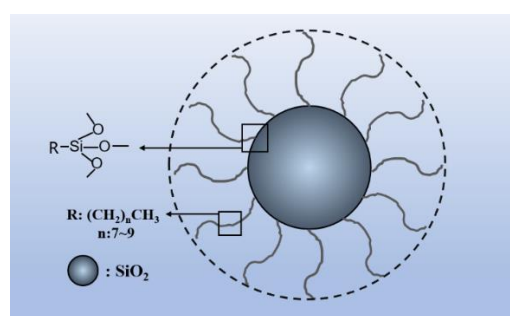


Figure 1. Schematic diagram of molecular structure of hybrid nanoSiO₂ (HNS).

2.2. Sample Preparation

Figure 2 shows the schematic diagram of applying the protective layer on the mortar substrate. The mortar substrate was first prepared by casting the well proportioned fresh mixture in a cubic mold with dimensions of 70 × 70 × 50 mm until initial setting. Then, SPMs with a thickness of 20 mm were coated on the top surface of the substrate. All the samples were cured in a standard chamber (20 ± 2 °C, 95% relative humidity) for 28 days. Two types of SPMs were adopted in this experiment. The formula of both substrates and SPMs are listed in Table 4. The FA, slag, and HNS were added by replacing the same dosage of cement. All the abbreviations used in this study were listed in Table 5.

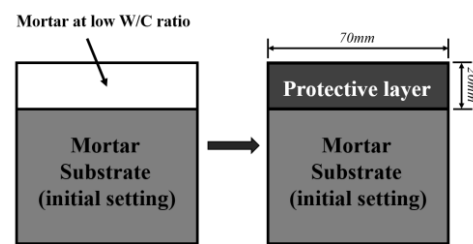


Figure 2. Schematic diagram of the process of applying the protective layer onto the mortar substrate.

Table 4. Mix proportions of substrate and different kinds of protective layers.

Parts	Water/Binder	Sand/Binder	FA(wt%)	Slag(wt%)	HNS(wt%)
SPM-0	0.40	3:1	15	15	0
SPM-1	0.40	3:1	15	15	1
Substrates	0.53	3:1	15	15	0

Table 5. Explanations of abbreviations.

Abbreviations	Content of Reference
SPMs	Srface protect materials
SCMs	Supplementary cementitious materials
NS	NanoSiO ₂
HNS	Hybrid nanoSiO ₂
FA	Fly ash
CH	Ca(OH) ₂
XRD	X-ray diffraction
TGA	Thermal gravimetric analysis
FTIR	Fourier-transform infrared spectroscopy
MIP	Mercury intrusion porosimeter
REF	Samples consist of substrates without SPM
N	Samples consist of substrates and SPM-0
HN	Samples consist of substrates and SPM-1

HN represents the samples covered with protective layers consisting of 1 wt% HNS; N represents the samples covered with protective layers consisting of 0 wt% HNS; REF represents the samples without protective layers.

2.3. Test Methods

2.3.1. Carbonation Depth

Five sides of samples were sealed with paraffin wax (as shown in Figure 3), and the surface covered with the protective layer was exposed to CO₂ at a concentration of (20 ± 2)% and relative humidity of (70 ± 5)% in a HTX-12X carbonation experiment chest manufactured by Suzhou Donghua Testing Instrument Co., Ltd. (Suzhou, China). The carbonation test procedure was in compliance with Chinese National Standard GBJ82-85.

After 28 days of carbonation, the samples were split into two halves, and a phenolphthalein alcohol solution was sprayed onto the fractured surface to identify the carbonation depth.

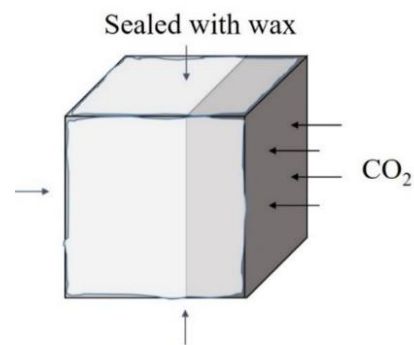


Figure 3. Direction of CO₂ diffusion during carbonation.

2.3.2. Chemical Composition

Specimens for chemical composition tests including XRD, TGA, and FTIR analysis were extracted from the SPMs within a 5 mm depth beneath the surface after carbonation and ceased hydration by immersing them into isopropanol for 48 h.

XRD was conducted to analyze the changes of mineral compositions of the SPMs before and after carbonation. A Bruker D8 Advance X-ray diffractometer (Bruker Technology Co., Ltd., Karlsruhe, Germany). was used, and the scanning range (2θ) was from 5° to 70° at a rate of $5^\circ/\text{min}$ in a θ - θ configuration using Cu-K α radiation.

TGA was carried out to investigate the mineral compositions of the SPMs before and after carbonation. Specimens for TGA were extracted from the carbonated area beneath the surface of SPMs and ground to powder followed by drying in 50°C for 24 h. The weighted powder samples were tested in a nitrogen atmosphere by a NETZSCH STA449F3 thermal analyzer (NETZSCH-Gerätebau GmbH, Selb, Germany), and were heated from 30 – 1000°C at a rate of $20^\circ\text{C}/\text{min}$.

FTIR was carried out to analyze the changes of chemical compositions of SPMs after carbonation, a Nicolet IS10 fourier transform infrared spectrometer (Thermo Fisher Scientific, Waltham, MA, USA). was used to conduct the FRIR test. The wavenumbers range was 2000 to 400 cm^{-1} at a resolution of 2 cm^{-1} . Each sample was scanned 32 times.

2.3.3. Pore Structures

To investigate the pore structures of different SPMs before carbonation, a Micrometrics AutoPore IV 9510 (American Michael Instruments Corp., Charlottesville, VA, USA) was used to conduct the MIP test with a maximum pressure of up to 415 MPa. Specimens for the MIP test were extracted from the SPMs within a 5 mm depth beneath the surface before carbonation, and then stopped hydration by immersing them into isopropanol for 48 h. Pore size distribution curves ranging from 3 – $360\text{ }\mu\text{m}$ were drawn out.

2.3.4. Thermodynamic Modeling

A Gibbs free energy minimization program was used to calculate the changes of the phase assemblage during carbonation in a chemical system. CEMDATA18 database was used [25].

3. Results and Discussion

3.1. Carbonation Depth

Figure 4 shows the carbonation depth of different samples after 28 days of carbonation. It can be seen that REF has the largest carbonation depth of about 14.3 mm. Such a high carbonation degree may be due to a porous surface structure caused by a relatively large W/C ratio of 0.53. It is well-known that the W/C ratio is a vital parameter affecting the density of cementitious materials. Normally, a larger W/C ratio results in a looser microstructure and thereby provides more diffusion channels for CO₂ [26]. Compared with REF, the carbonation depth of group N (4.5 mm) and HN (3mm) is reduced by 69.2% and 79.0%, respectively. Apparently, the application of protective layers together with a low

W/C ratio results in both a denser surface and a less amount of connected pores, impeding the diffusion of CO_2 and elevating the carbonation resistance. The highest carbonation resistance of HN may due to the pozzolanic reaction between HNS and $\text{Ca}(\text{OH})_2$, leading to the formation of dense C-S-H and the consumption of $\text{Ca}(\text{OH})_2$. This is because C-S-H is beneficial to densifying the microstructure of cement paste, while the presence of less $\text{Ca}(\text{OH})_2$ decelerates the carbonation reaction. Moreover, the filling effect of nanoSiO_2 is also believed to be conducive to reducing the porosity.

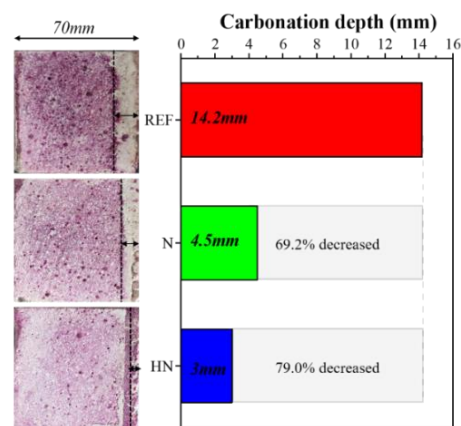


Figure 4. Carbonation depth of different samples after 28 days of carbonation.

From the results above, it can be concluded that the combination of a protective layer with a low W/C ratio can effectively reduce the carbonation of traditional cement-based materials. Interestingly, the use of HNS can further enhance this protective effect by the induced pozzolanic reaction and filling effect.

3.2. XRD

The XRD patterns of different samples after 28 days of carbonation are shown in Figure 5. The appearance of quartz peaks in Figure 5a is attributed to the presence of sand in the powdered samples, which is hard to be completely eliminated before the XRD test. Typical calcite peaks can be observed at 24.1° , 29.5° , 36.6° , and 39.5° . Obviously, REF has the highest content of calcite, while N has the lowest calcite content.

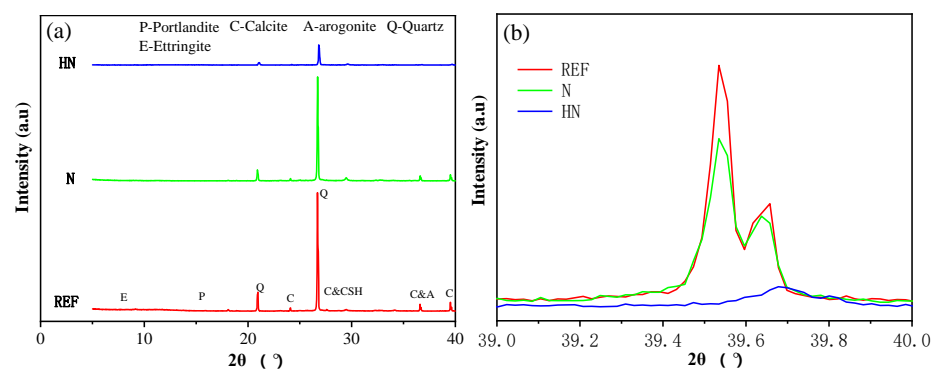


Figure 5. XRD patterns of different samples after carbonation: (a) overall patterns and (b) partial enlarged view of patterns near 39° .

Figure 5b shows the partial enlarged view of patterns near 39° with two remarkable calcite peaks. The calcite peaks at 39.5° and 39.6° reveal the highest carbonation degree of REF. Compared with REF, N experiences a drop in the calcite content. Moreover, the calcite peaks in HN are almost unobservable. A decrease of calcite in HN and N points to a better anti-carbonation performance compared with REF. The highest carbonation resistance of

HN may be due to the previously mentioned improvement in the pore structures caused by the filling effect of HNS and the formation of dense C–S–H as a result of the pozzolanic reaction between HNS and CH. Plus, the consumption of CH by the pozzolanic reaction directly reduces the formation of calcite.

3.3. FTIR

The FTIR spectra patterns (ranging from 2000–400 cm^{-1}) of different samples are given in Figure 6. In each curve, three gray areas are used to highlight three bands: the band at 1440 cm^{-1} corresponds to $\nu_3\text{-CO}_3^{2-}$, the band at 875 cm^{-1} corresponds to $\nu_2\text{-CO}_3^{2-}$, and the band at 712 cm^{-1} corresponds to $\nu_4\text{-CO}_3^{2-}$. The intensity of these three bands is in an increasing order of $\text{REF} < \text{HN} < \text{N}$. The band at 712 cm^{-1} is almost invisible in HN. A decrease in the band intensity reflects a decrease in the CaCO_3 content and a corresponding improvement in the carbonation resistance. The FTIR analysis demonstrates that HN has the best carbonation resistance.

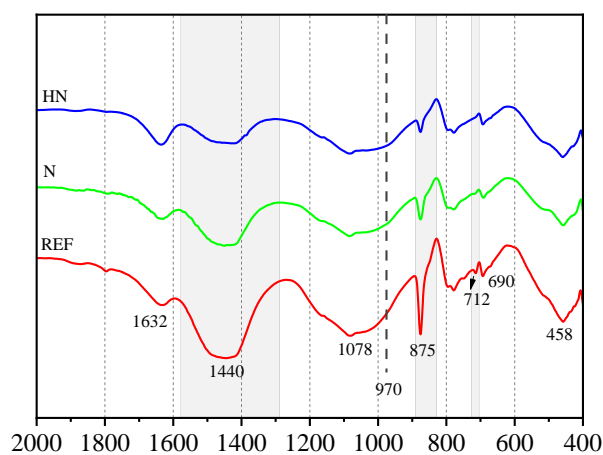


Figure 6. FTIR patterns of different samples after carbonation.

The dashed line in Figure 6 locates in a position at 970 cm^{-1} , which represents a band corresponding to the Si–O stretching vibration in C–S–H. At a Ca/Si of ≈ 1.7 , the frequency of this band will increase along with the decalcification of C–S–H [27]. In Figure 6, the bands near 970 cm^{-1} in all the three patterns shift to a higher frequency area at 1078 cm^{-1} , while the position at 1080 cm^{-1} corresponds to amorphous silica gel, which is the final product of the decalcified reaction of C–S–H. This observation indicates the occurrence of different degrees of C–S–H decalcification: the stronger band at 1078 cm^{-1} reflects a larger content of amorphous silica gel and indicates a higher degree of decalcification. Taken together, the decalcification degree of different samples is in the decreasing order of $\text{HN} < \text{N} < \text{REF}$. The lower decalcification degree of HN could be attributed to the dense microstructure of C–S–H gels, further supporting the improved carbonation resistance induced by the incorporation of HNS.

The band at 1632 cm^{-1} is assigned to the bending vibration of H–O–H in chemical bound water in hydration products [28]. A decrease in the intensity of this band reflects the consumption of hydration products and a corresponding increase in the carbonation degree. The presence of the most remarkable band at 1632 cm^{-1} in Figure 6 once again confirms the best carbonation resistance of HN.

3.4. TG

The results of (Thermal Gravimetric Analysis) TGA of different samples carbonated for 28 days are shown in Figure 7. Mass loss peaks of different mineral compositions are observed in different temperature ranges: the peaks in the range of 100–380 $^{\circ}\text{C}$ correspond to the dehydration of C–S–H/Aft and the peaks within 380–460 $^{\circ}\text{C}$ correspond to the dihy-

droxylation of $\text{Ca}(\text{OH})_2$ (Equation (3)); the peaks emerging from 460–750 °C correspond to the decomposition of CaCO_3 (Equation (4)).



$$m(\text{CaCO}_3) = \frac{M(\text{CaCO}_3)}{M(\text{CO}_2)} \times m(\text{CO}_2) \quad (5)$$

$$m(\text{Ca}(\text{OH})_2) = \frac{M(\text{Ca}(\text{OH})_2)}{M(\text{H}_2\text{O})} \times m(\text{H}_2\text{O}) \quad (6)$$

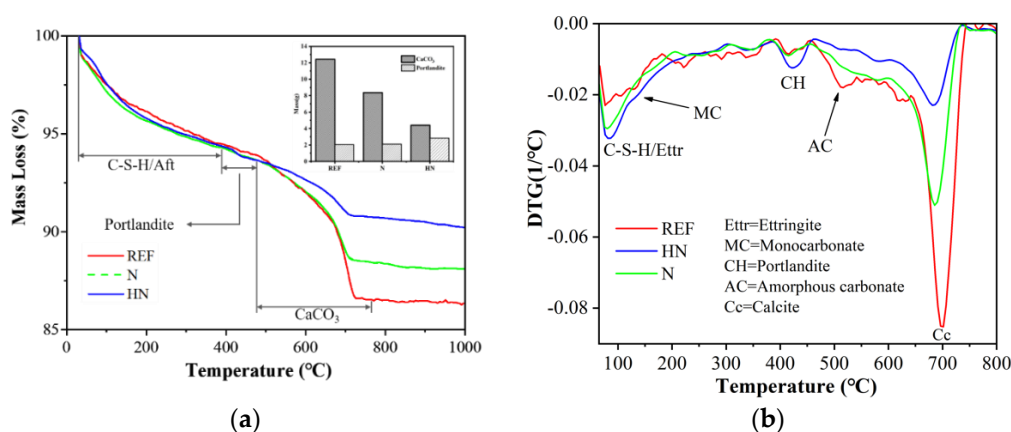


Figure 7. TG and DTG curves for different samples after carbonated for 28 days: (a) TG and (b) DTG.

Figure 7a shows the mass loss curves measured by TG, and the histogram in the legend presents the content of $\text{Ca}(\text{OH})_2$ and CaCO_3 calculated by Equations (5) and (6), which is summarized in Table 6. The content of CaCO_3 in N and HN decreases by 32.60% and 64.47% relative to REF, respectively, indicating a decrease in the capacity of CO_2 absorption with the incorporation of HNS. This conclusion is further supported by the presence of a higher content of CH in HN compared with N and REF.

Table 6. Content of CaCO_3 and $\text{Ca}(\text{OH})_2$ in different samples after carbonation.

Components	REF	N	HN
CaCO_3 (wt%)	12.42	8.37	4.40
$\text{Ca}(\text{OH})_2$ (wt%)	2.05	2.11	2.85

As can be seen from Figure 7b, the peak of CaCO_3 in REF extends to the low temperature area, and a small peak appears at about 500 °C, which probably corresponds to amorphous carbonates due to incomplete crystallization under a high degree of carbonation [29]. The presence of amorphous carbonates may be attributed to the carbonation of hydration products, such as C–S–H and ettringite [30,31]. These observations are consistent with the results of the FTIR analysis, demonstrating a lower degree of decalcification in the samples with a protective layer and the incorporation of HNS.

The observed lower carbonation degree of HN is possibly due to the following two reasons: (a) The filling effect of HNS improves the pore structure and reduces the amount of connected pores, effectively impeding the CO_2 diffusion; (b) The formation of secondary C–S–H induced by the seeding effect of HNS further densifies the microstructure of the protective layer and thereby enhances the resistance to CO_2 diffusion. As shown in Figure 8, the accumulation of C–S–H on the surface of cement particles can effectively reduce the contact between the un-hydrated cement and water, thus retarding the migration

of Ca^{2+} [32,33]. Under such a circumstance, the concentration of Ca^{2+} might be further decreased due to the consumption by carbonation. Thus, the subsequent precipitation of CaCO_3 becomes more difficult.

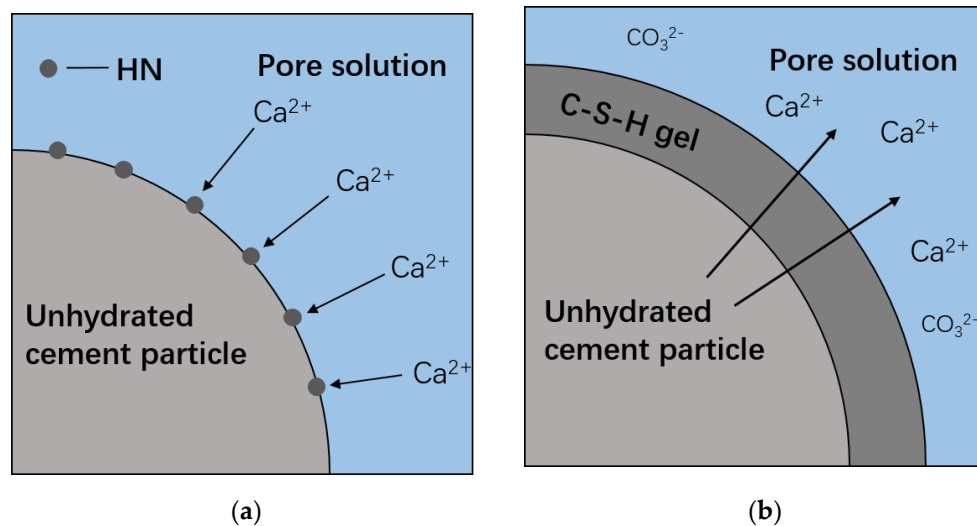


Figure 8. Schematic diagram of Ca^{2+} migration: (a) during hydration and (b) during carbonation.

3.5. Pore Structures

Figure 9 shows the pore size distribution of different samples. Obviously, REF has the largest total porosity compared with N and HN due to its high W/C ratio. With the addition of HNS, HN has the lowest porosity. Pore volumes at different diameters for different samples are shown in Figure 10. Generally, the pores in concrete are classified into four categories: gel pores (≤ 10 nm), transition pores (10–100 nm), capillary pores (100–1000 nm), and big pores (>1000 nm) [34,35]. Big pores and capillary pores are harmful to the cement-based materials because they are the main diffusion channels for corrosive medium diffusion. It can be seen from Figure 10 that compared with REF, the volume of big pores in N and HN is decreased by 7.9% and 48.3%, respectively, while the volume of capillary pores in N and HN is, respectively, decreased by 38.2% and 58.5%. These results well demonstrate that the addition of HNS in cementitious materials not only reduces the total porosity but also refines the pore structures. The formation of secondary C–S–H induced by HNS fills in the voids between cement grains, resulting in the improvement of microstructures.

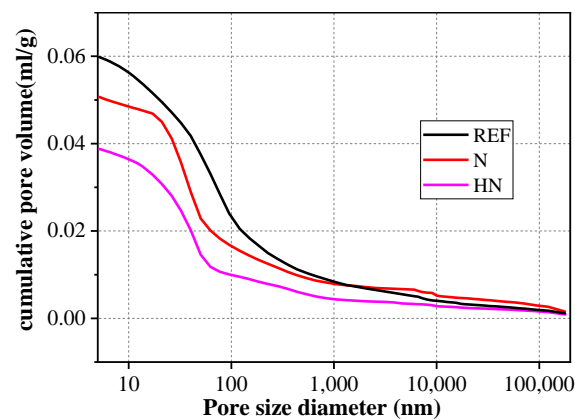


Figure 9. Pore size distribution of different samples.

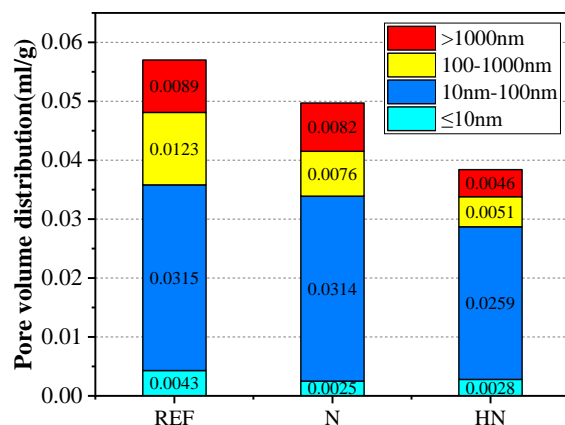


Figure 10. Pore volumes of different samples at different diameters.

3.6. Thermodynamic Modeling

Figure 11 shows the phase assemblage changes of two different blends in contact with CO₂ predicted by thermodynamic modeling. The ordinate represents the volume percentage of original solid phases as a function of the CO₂ content. As can be seen from Figure 11, N and HN display a similar graph, indicating that HNS has a negligible effect on the total volumes of each phase. It is worth noting that CH is not observed due to the SCMs induced pozzolanic reaction. This result is not consistent with previous studies. It is possible that the added SCMs are not completely reacted with cement in actual situations. Meanwhile, the stratlingite and high-Ca C–S–H become the dominating phases in a non-CO₂ situation. As the CO₂ content increases, stratlingite and C–S–H are consumed along with the formation of decalcified C–S–H, calcite and gibbsite.

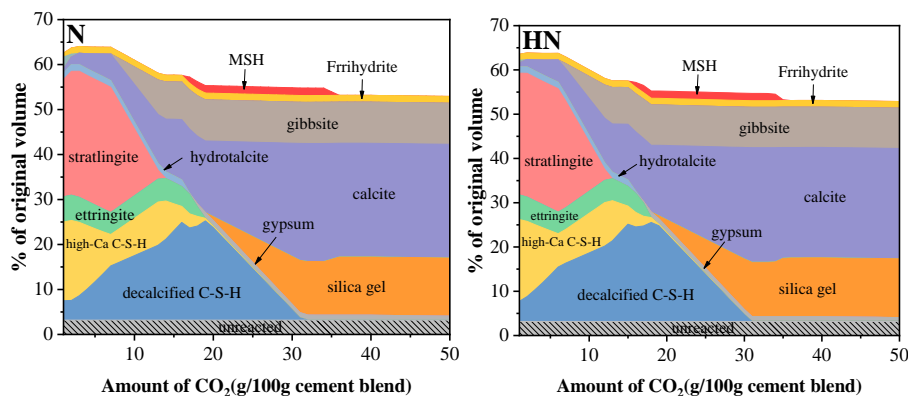


Figure 11. Changes of phase assemblage of N and HN samples.

Changes of pH and Ca/Si ratio of two blends in contact with CO₂ are shown in Figure 12. Two remarkable platforms are observed, which correspond to the consumption of stratlingite and decalcified C–S–H, respectively. This observation indicates that stratlingite and decalcified C–S–H can maintain a stable Ca/Si ratio and pH during carbonation. Thus, a high content of C–S–H and stratlingite may be beneficial to preventing the decrease of pH in cement-based materials upon contact with CO₂. This helps explain why the HNS incorporated samples possess better carbonation resistance in practical applications.

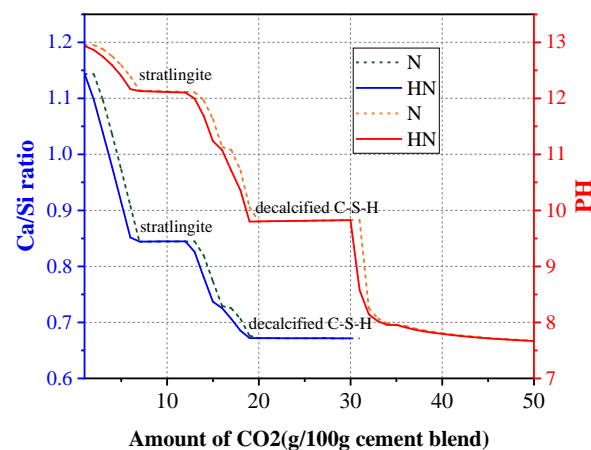


Figure 12. Changes of Ca/Si ratio and pH in contact with CO₂.

It can also be observed that the slope absolute values of both curves become smaller along with the decrease of the Ca/Si ratio, suggesting that a relatively smaller Ca/Si ratio is not conducive to decalcification. Therefore, the incorporation of HNS in cementitious materials is likely to retard the decalcification of C–S–H and stratlingite by increasing the Si/Ca ratio.

4. Conclusions

In this study, surface protective materials (SPM) with hybrid nanoSiO₂ (HNS) were prepared and applied on the surface of mortar substrates. The carbonation resistance of SPMs was investigated, and HNS was found to be effective in enhancing the carbonation resistance of cement mortar. The main conclusions can be drawn as follows:

1. The use of SPMs effectively increased the carbonation resistance of the substrates. Compared with REF, the carbonation depth of N and HN was reduced by 69.2% and 79.0%, respectively.
2. The combination of HNS with SPMs further enhanced the carbonation resistance. Compared with the SPMs without HNS, the carbonation depth of the HNS incorporated SPMs was reduced from 4.5 to 3 mm.
3. The incorporation of HNS in SPMs refined the pore structures. Compared with the SPMs without HNS, the HNS incorporated SPMs experienced a 43.9% and 32.9% reduction in big pores and capillary pores, respectively. This was ascribed to the formation of extra C–S–H and the filling effect of nanoparticles.
4. From thermodynamic modeling, it can be observed that the introduction of HNS could promote the formation of C–S–(A)–H, prevent the decrease of pH in pore solution, and lower the Ca/Si ratio of C–S–(A)–H. These effects are beneficial to augmenting the carbonation resistance of SPMs.

Overall, this study verified the enhancing effect of HNS on the carbonation resistance of cement mortar. However, the synergistic effect of HNS and SCMs, such as fly ash and slag, merits further research.

Author Contributions: Article writing, experimental data analysis, K.X.; methodology, Y.G.; conceptualization, L.J.; review and editing, M.G.; Software operation, L.C. processing experimental data, F.H. All authors have read and agreed to the published version of the manuscript.

Funding: This research was funded by the National Natural Science Foundation of China (Grant Nos.51808188).

Data Availability Statement: The data used to support the findings of this study are available from the corresponding author upon request.

Acknowledgments: The authors thank Jiangsu Research Institute of Building Science Co., Ltd.

Conflicts of Interest: The authors declare that they have no known competing financial interest or personal relationships that could have appeared to influence the work reported in this paper.

References

1. Zhan, B.; Poon, C.; Shi, C. CO₂ curing for improving the properties of concrete blocks containing recycled aggregates. *Cem. Concr. Compos.* **2013**, *42*, 1–8. [[CrossRef](#)]
2. Thomas, J.J.; Biernacki, J.J.; Bullard, J.W.; Bishnoi, S.; Dolado, J.S.; Scherer, G.W.; Luttge, A. Modeling and simulation of cement hydration kinetics and microstructure development. *Cem. Concr. Res.* **2011**, *41*, 1257–1278. [[CrossRef](#)]
3. Xi, F.; Davis, S.J.; Ciais, P.; Crawford-Brown, D.; Guan, D.; Pade, C.; Shi, T.; Syddall, M.; Lv, J.; Ji, L.; et al. Substantial global carbon uptake by cement carbonation. *Nat. Geosci.* **2016**, *9*, 880–883. [[CrossRef](#)]
4. Andres, R.J.; Boden, T.A.; Bréon, F.M.; Ciais, P.; Davis, S.; Erickson, D.; Gregg, J.S.; Jacobson, A.; Marland, G.; Miller, J.; et al. A synthesis of carbon dioxide emissions from fossil-fuel combustion. *Biogeosciences* **2015**, *9*, 1845–1871. [[CrossRef](#)]
5. Richardson, M.G. *Fundamentals of Durable Reinforced Concrete*; Spon Press: New York, NY, USA, 2002.
6. Shah, V.; Scrivener, K.; Bhattacharjee, B.; Bishnoi, S. Changes in microstructure characteristics of cement paste on carbonation. *Cem. Concr. Res.* **2018**, *109*, 184–197. [[CrossRef](#)]
7. Seneviratne, A.M.G.; Sergi, G.; Page, C.L. Performance characteristics of surface coatings applied to concrete for control of reinforcement corrosion. *Constr. Build. Mater.* **2000**, *14*, 55–59. [[CrossRef](#)]
8. Ibrahim, M. Effectiveness of concrete surface treatment materials in reducing chloride-induced reinforcement corrosion. *Constr. Build. Mater.* **1997**, *11*, 443–451. [[CrossRef](#)]
9. Papadakis, V.G. Effect of supplementary cementing materials on concrete resistance against carbonation and chloride ingress. *Cem. Concr. Res.* **2000**, *30*, 291–299. [[CrossRef](#)]
10. Xue, L.; Zhang, Z.; Wang, H. Hydration mechanisms and durability of hybrid alkaline cements (HACs): A review. *Constr. Build. Mater.* **2021**, *266*, 121039. [[CrossRef](#)]
11. Parron-Rubio, M.E.; Perez-Garcia, F.; Gonzalez-Herrera, A.; Oliveira, M.J.; Rubio-Cintas, M.D. Slag substitution as a cementing material in concrete: Mechanical, physical and environmental properties. *Materials* **2019**, *12*, 2845. [[CrossRef](#)]
12. Lam, L.; Wong, Y.L.; Poon, C.S. Degree of hydration and gel/space ratio of high-volume fly ash/cement systems. *Constr. Build. Mater.* **2000**, *30*, 747–756. [[CrossRef](#)]
13. Yehdego, T.; Peethamparan, S. The role of nano silica in modifying the early age hydration kinetics of binders containing high volume fly ashes. In *Nanotechnology in Construction*; Springer International Publishing: Cham, Switzerland, 2015; pp. 399–405.
14. Gu, Y.; Ran, Q.; She, W.; Liu, J. Modifying Cement Hydration with NS@PCE Core-Shell Nanoparticles. *Adv. Mater. Sci. Eng.* **2017**, *2017*, 1–13. [[CrossRef](#)]
15. Shah, S.P.; Hou, P.; Konsta-Gdoutos, M.S. Nano-modification of cementitious material: Toward a stronger and durable concrete. *J. Sustain. Cem. Based Mater.* **2016**, *5*, 1–22. [[CrossRef](#)]
16. Du, H.; Du, S.; Liu, X. Durability performances of concrete with nano-silica. *Constr. Build. Mater.* **2014**, *73*, 705–712. [[CrossRef](#)]
17. Thomas, J.J.; Jennings, H.M.; Chen, J.J. Influence of nucleation seeding on the hydration mechanisms of tricalcium silicate and cement. *J. Phys. Chem. C* **2009**, *113*, 4327–4334. [[CrossRef](#)]
18. Sandrolini, F.; Franzoni, E.; Pigino, B. Ethyl silicate for surface treatment of concrete—Part I: Pozzolanic effect of ethyl silicate. *Cem. Concr. Compos.* **2012**, *34*, 306–312. [[CrossRef](#)]
19. Hou, P.; Qian, J.; Cheng, X.; Shah, S.P. Effects of the pozzolanic reactivity of nanoSiO₂ on cement-based materials. *Cem. Concr. Compos.* **2015**, *55*, 250–258. [[CrossRef](#)]
20. Hou, P.; Cheng, X.; Qian, J.; Zhang, R.; Cao, W.; Shah, S.P. Characteristics of surface-treatment of nano-SiO₂ on the transport properties of hardened cement pastes with different water-to-cement ratios. *Cem. Concr. Compos.* **2015**, *55*, 26–33. [[CrossRef](#)]
21. Ghafari, E.; Costa, H.; Júlio, E.; Portugal, A.; Durães, L. The effect of nanosilica addition on flowability, strength and transport properties of ultra high performance concrete. *Mater. Eng.* **2014**, *59*, 1–9. [[CrossRef](#)]
22. Gu, Y.; Ran, Q.; Shu, X.; Yu, C.; Chang, H.; Liu, J. Synthesis of nanoSiO₂@PCE core-shell nanoparticles and its effect on cement hydration at early age. *Constr. Build. Mater.* **2016**, *114*, 673–680. [[CrossRef](#)]
23. Collodetti, G.; Gleize, P.J.P.; Monteiro, P.J.M. Exploring the potential of siloxane surface modified nano-SiO₂ to improve the Portland cement pastes hydration properties. *Constr. Build. Mater.* **2014**, *54*, 99–105. [[CrossRef](#)]
24. Mora, E.; González, G.; Romero, P.; Castellón, E. Control of water absorption in concrete materials by modification with hybrid hydrophobic silica particles. *Constr. Build. Mater.* **2019**, *221*, 210–218. [[CrossRef](#)]
25. Lothenbach, B.; Kulik, D.A.; Matschei, T.; Balonis, M.; Baquerizo, L.; Dilnesa, B.; Miron, G.D.; Myers, R.J. Cemdata18: A chemical thermodynamic database for hydrated Portland cements and alkali-activated materials. *Cem. Concr. Res.* **2019**, *115*, 472–506. [[CrossRef](#)]
26. Siddique, S.; Naqi, A.; Jang, J.G. Influence of water to cement ratio on CO₂ uptake capacity of belite-rich cement upon exposure to carbonation curing. *Cem. Concr. Compos.* **2020**, *111*, 103616. [[CrossRef](#)]
27. Pan, X.; Shi, C.; Farzadnia, N.; Hu, X.; Zheng, J. Properties and microstructure of CO₂ surface treated cement mortars with subsequent lime-saturated water curing. *Cem. Concr. Compos.* **2019**, *99*, 89–99. [[CrossRef](#)]
28. Chen, T.; Gao, X. Effect of carbonation curing regime on strength and microstructure of Portland cement paste. *J. CO₂ Utilization* **2019**, *34*, 74–86. [[CrossRef](#)]

29. Šauman, Z. Carbonization of porous concrete and its main binding components. *Cem. Concr. Res.* **1971**, *1*, 645–662. [[CrossRef](#)]
30. Rostami, V.; Shao, Y.; Boyd, A.J.; He, Z. Microstructure of cement paste subject to early carbonation curing. *Cem. Concr. Res.* **2012**, *42*, 186–193. [[CrossRef](#)]
31. Shi, Z.; Lothenbach, B.; Geiker, M.R.; Kaufmann, J.; Leemann, A.; Ferreira, S.; Skibsted, J. Experimental studies and thermodynamic modeling of the carbonation of Portland cement, metakaolin and limestone mortars. *Cem. Concr. Res.* **2016**, *88*, 60–72. [[CrossRef](#)]
32. Li, R.; Hou, P.; Xie, N.; Ye, Z.; Cheng, X.; Shah, S.P. Design of SiO₂/PMHS hybrid nanocomposite for surface treatment of cement-based materials. *Cem. Concr. Compos.* **2018**, *87*, 89–97. [[CrossRef](#)]
33. Powers, T.C. Structure and physical properties of hardened portland cement paste. *J. Am. Ceram. Soc.* **1958**, *41*, 1–6. [[CrossRef](#)]
34. Jennings, H.M.; Kumar, A.; Sant, G. Quantitative discrimination of the nano-pore-structure of cement paste during drying: New insights from water sorption isotherms. *Cem. Concr. Res.* **2015**, *76*, 27–36. [[CrossRef](#)]
35. Wang, Q.; Li, S.; Pan, S.; Cui, X.; Corr, D.J.; Shah, S.P. Effect of graphene oxide on the hydration and microstructure of fly ash-cement system. *Constr. Build. Mater.* **2019**, *198*, 106–119. [[CrossRef](#)]